

# Towards Quantum Accelerated Large-scale Topology Optimization

Zisheng Ye<sup>1</sup> and Wenxiao Pan<sup>\*1</sup>

<sup>1</sup>Department of Mechanical Engineering, University of Wisconsin-Madison, Madison, WI 53706, USA

## Abstract

We present a new method that efficiently solves TO problems and provides a practical pathway to leverage quantum computing to exploit potential quantum advantages. This work targets on large-scale, multi-material TO challenges for three-dimensional (3D) continuum structures, beyond what have been addressed in prior studies. Central to this new method is the modified Dantzig-Wolfe (MDW) decomposition, which effectively mitigates the escalating computational cost associated with using classical Mixed-Integer Linear Programming (MILP) solvers to solve the master problems involved in TO, by decomposing the MILP into local and global sub-problems. Evaluated on 3D bridge designs, our classical implementation achieves comparable solution quality to state-of-the-art TO methods while reducing computation time by orders of magnitude. It also maintains low runtimes even in extreme cases where classical MILP solvers fail to converge, such as designs involving over 50 million variables. The computationally intensive local sub-problems, which are essentially Binary Integer Programming (BIP) problems, can potentially be accelerated by quantum computing via their equivalent Quadratic Unconstrained Binary Optimization (QUBO) formulations. Enabled by the MDW decomposition, the resulting QUBO formulation requires only sparse qubit connectivity and incurs a QUBO construction cost that scales linearly with problem size, potentially accelerating BIP sub-problem solutions by an additional order of magnitude. Due to limited access to quantum hardware, the validity of the formulated QUBO is verified using the Quantum Approximate Optimization Algorithm (QAOA). All observed and estimated speedups become increasingly significant with larger problem sizes and when moving from single-material to multi-material designs. This suggests that this new method, along with quantum computing, will play an increasingly valuable role in addressing the scale and complexity of real-world TO applications.

**Keywords:** Mixed-integer nonlinear programming; Mixed-integer linear programming; Binary integer programming; Quadratic unconstrained binary optimization; Topology optimization; Quantum computing

## 1 Introduction

Spanning diverse sectors, from structural mechanics [1], fluid dynamics [2–4], electromagnetics [5], and photonics [6] to multiphysics applications [7–9], and from automotive [10] to aerospace [11] industries, there is a growing need for designing high-performance, energy-efficient, and lightweight components, devices, and structures. Topology optimization (TO) has emerged as a powerful computational tool to address this need. It determines the optimal distribution of material within a given design domain to maximize structural or functional performance while satisfying the governing physics and design constraints. TO can

---

\*Corresponding author. Email: [wpan9@wisc.edu](mailto:wpan9@wisc.edu)

address discrete truss structures, where the design is of finite dimensions and defined by a finite set of parameters, or continuum structures, where designs are represented as distributed functions. This work focuses on the latter, because it poses greater computational and theoretical challenges. In continuum TO, the governing physics, whether structural mechanics, fluid dynamics, or multiphysics, are typically enforced via state equilibrium equations in the form of partial differential equations (PDEs). When subject to design constraints, e.g., constraining total volume or material usage, the resulting formulation becomes a PDE-constrained optimization problem. The expanding application of TO has brought about substantial computational challenges. These arise from the high-dimensional and complex design space, the intensive cost of solving PDEs, and the need to repeatedly solve PDEs throughout the optimization process. Two key factors largely determine the total computing time: the number of iterations required to achieve convergence, which dictates the number of PDE solver calls; and the time needed to solve the optimization subproblem at each iteration. Therefore, advancing computational methodologies and frameworks to improve TO solution efficiency should focus on reducing iteration counts and accelerating per-iteration solution time.

As a PDE-constrained optimization problem, TO requires discretizing the design domain, typically via finite element methods (FEM), with each element representing a potential material site. This results in an optimization problem with a substantial number of binary (0/1) design variables, where 1 indicates material presence and 0 its absence. The nonlinear dependence of continuous state variables on these binary variables formulates TO as large-scale Mixed-Integer Nonlinear Programming (MINLP) problems, constrained by equality and inequality constraints. Being NP-hard in general [12], these problems are computationally intensive using traditional methods [13–19]. Our prior work introduced a TO framework [20] that significantly enhances computational efficiency by reducing optimization iterations and, consequently, the frequency of PDE solving. This framework integrates generalized Benders’ decomposition [21] with adaptive trust regions, formulating the master sub-problem (derived from the MINLP problem) as a multi-cut Mixed-Integer Linear Programming (MILP) problem. This approach enables estimation of the original objective function’s upper and lower bounds, accelerating solution convergence for both convex and non-convex problems across single- and multi-material designs. Compared to widely used traditional methods such as Solid Isotropic Material with Penalty (SIMP) [13], Floating Projection (FP) [17], and Sequential Approximate Integer Programming (SAIP) [18], this framework significantly reduces the number of optimization iterations and FEM analyses required, while achieving similar objective function values and optimized topologies. To scale this framework to larger TO problems, advancements to the MILP solver are required. Quantum computing, an emerging paradigm, offers potential superiority over classical computing for combinatorial optimization tasks [22–27]. For example, quantum annealing can accelerate the search for global minima in quadratic unconstrained binary optimization (QUBO) problems by enabling faster escape from local optima [28, 29]. However, directly converting a MILP problem into an equivalent QUBO problem introduces new challenges. In TO, some design constraints often translate into global constraints within the MILP, which involve all design variables. When mapped into the QUBO formulation, these global constraints produce a dense Hamiltonian, i.e., a QUBO with a densely populated coefficient matrix. This not only imposes the need for all-to-all qubit connectivity, which exceeds the capabilities of most near-term quantum hardware [30–32], but also leads to high pre-processing costs. Specifically, constructing the QUBO’s dense coefficient matrix scales quadratically with the number of design variables, diminishing the overall efficiency and offsetting any potential quantum speedup.

Therefore, this paper introduces a new method that significantly enhances the efficiency and scalability of solving MILP problems arising from large-scale TO. It also offers a practical pathway to harness quantum advantages by requiring only sparse qubit connectivity and ensuring that the cost of constructing QUBO scales linearly with problem size. This new method centers on a modified Dantzig-Wolfe (MDW) decomposition. Utilizing its block-angular structure, the MILP problem is decomposed into a series of reduced-size sub-problems, which are categorized as global or local, corresponding to global and local constraints, respectively. Unlike the standard Dantzig-Wolfe decomposition [33], the MDW formulation is designed to effectively control the size of the global sub-problem. The local sub-problems, which account for the majority of the computational cost, are essentially Binary Integer Programming (BIP) problems and can potentially be ac-

celerated using quantum computing by translating them into equivalent QUBO problems. Importantly, each local sub-problem involves only local constraints, resulting in QUBO formulations with sparse Hamiltonians. This sparsity eliminates the need for all-to-all qubit connectivity, making the approach well-suited to near-term quantum hardware. Moreover, since each local sub-problem is independent, all QUBOs can be solved in parallel within each MDW iteration, enabling substantial gains in computational speed.

This work represents a distinct advancement over previous efforts that applied quantum computing to TO for improving computational efficiency. Unlike earlier studies limited to discrete truss structures [34, 35], which represent a small fraction of TO applications, this work addresses more challenging continuum structures. It also surpasses previous work, including our own [21] and others [36], which focused on small-scale, single-material designs and formulated QUBOs with dense Hamiltonians, necessitating all-to-all qubit connectivity and incurring quadratically scaled QUBO construction costs with increasing design variables.

## 2 Preliminary

### 2.1 Formulation of Discrete Variable Topology Optimization (DVTO)

Consider the design of structures within a continuum domain ( $\Omega$ ), for which the design of material distribution is represented by an indicator function  $\rho(\mathbf{x})$  with  $\mathbf{x} \in \Omega$  [37]. The physical equilibrium state of the structures is governed by a partial differential equation (PDE) subject to appropriate boundary conditions (BCs). In the context of designing structures governed by linear elasticity, the governing PDE is given by:

$$\begin{aligned} \nabla \cdot \boldsymbol{\sigma}(\mathbf{u}) + \mathbf{b} &= \mathbf{0} & \text{in } \Omega, \\ \boldsymbol{\sigma}(\mathbf{u}) \cdot \mathbf{n} &= \mathbf{h}_\Gamma & \text{on } \Gamma_N, \\ \mathbf{u} &= \mathbf{u}_\Gamma & \text{on } \Gamma_D, \end{aligned} \quad (1)$$

where  $\boldsymbol{\sigma}(\mathbf{u}) = \mathbb{C} : \boldsymbol{\varepsilon}(\mathbf{u})$  is the stress tensor (2nd order);  $\mathbb{C}$  is the fourth-order elasticity tensor;  $\boldsymbol{\varepsilon} = \frac{1}{2}(\nabla \mathbf{u} + \nabla \mathbf{u}^\top)$  is the strain tensor (2nd order);  $\mathbf{b}$  denotes the body force; and  $\Gamma = \partial\Omega$  denotes the entire boundary of the design domain with  $\Gamma_D$  and  $\Gamma_N$  representing the portions where Dirichlet and Neumann BCs are imposed, respectively. Following numerical discretization of the above PDE (e.g., via FEM), the continuum TO problem in its discrete form can be expressed as:

$$\begin{aligned} \min_{\mathbf{u}, \boldsymbol{\rho}} \quad & f(\mathbf{u}, \boldsymbol{\rho}) \\ \text{s.t.} \quad & \mathbf{K}(\boldsymbol{\rho})\mathbf{u} = \mathbf{f} \\ & H_{i_H}(\boldsymbol{\rho}) \leq 0, \quad i_H = 1, \dots, n_H, \\ & \mathbf{u} \in \mathbb{R}^{3n_v}, \boldsymbol{\rho} \in \{0, 1\}^{n_e \times n_M} \end{aligned} \quad (2)$$

where  $\mathbf{f}$  encompasses the discretized source terms and BCs;  $\mathbf{u} = \{\mathbf{u}_v\}$  with  $\mathbf{u}_v = \{u_v, v_v, w_v\}$  denoting the nodal displacement on each vertex of the FEM mesh;  $\boldsymbol{\rho} = \{\rho_{e,m}\}$  with  $\rho_{e,m}$  denoting the design variable defined at the centroid of each element  $e$  in the mesh and for the candidate material  $m$ ;  $H_{i_H}$  denotes the inequality constraints that only exerted on design variables  $\boldsymbol{\rho}$ ; and  $\mathbf{K}$  is the linear operator discretized from Eq. (1). The mesh consists of  $n_v$  nodal points (or vertices) and  $n_e$  elements, with the design subject to  $n_M$  candidate materials and  $n_H$  inequality constraints.

When using FEM to discretize the governing equation in (1), the strain tensor  $\boldsymbol{\varepsilon}_e$  on each element  $e$  is

calculated from the nodal displacement  $\mathbf{u}_v$  as:

$$\begin{aligned}\boldsymbol{\varepsilon}_e &= \begin{bmatrix} \frac{\partial u_v}{\partial x} & \frac{\partial v_v}{\partial y} & \frac{\partial w_v}{\partial z} & \frac{\partial u_v}{\partial y} + \frac{\partial v_v}{\partial x} \\ \frac{\partial u_v}{\partial z} + \frac{\partial w_v}{\partial x} & \frac{\partial v_v}{\partial z} + \frac{\partial w_v}{\partial y} \end{bmatrix}^\top \\ &= \begin{bmatrix} \frac{\partial}{\partial x} & 0 & 0 & \frac{\partial}{\partial y} & \frac{\partial}{\partial z} & 0 \\ 0 & \frac{\partial}{\partial y} & 0 & \frac{\partial}{\partial x} & 0 & \frac{\partial}{\partial z} \\ 0 & 0 & \frac{\partial}{\partial z} & 0 & \frac{\partial}{\partial x} & \frac{\partial}{\partial y} \end{bmatrix}^\top \begin{bmatrix} u_v \\ v_v \\ w_v \end{bmatrix} \\ &= \mathbf{B}\mathbf{u}_v ,\end{aligned}\tag{3}$$

where  $\mathbf{B}$  is the strain-displacement matrix. The elemental stiffness matrix  $\mathbf{K}_e$  is then calculated from the elemental elasticity tensor  $\mathbb{C}_e$  as:

$$\mathbf{K}_e = \int_{\Omega_e} \mathbf{B}^\top \mathbb{C}_e \mathbf{B} d\Omega ,\tag{4}$$

where

$$\mathbb{C}_e = \sum_{m=1}^{n_M} \rho_{e,m} \mathbb{C}_m ,\tag{5}$$

with the elasticity tensor  $\mathbb{C}_m$  in 3D written as:

$$\begin{aligned}\mathbb{C}_m &= \frac{E_m}{(1 + \nu_m)(1 - 2\nu_m)} \times \\ &\begin{bmatrix} 1 - \nu_m & \nu_m & \nu_m & 0 & 0 & 0 \\ \nu_m & 1 - \nu_m & \nu_m & 0 & 0 & 0 \\ \nu_m & \nu_m & 1 - \nu_m & 0 & 0 & 0 \\ 0 & 0 & 0 & \frac{1-2\nu_m}{2} & 0 & 0 \\ 0 & 0 & 0 & 0 & \frac{1-2\nu_m}{2} & 0 \\ 0 & 0 & 0 & 0 & 0 & \frac{1-2\nu_m}{2} \end{bmatrix} .\end{aligned}\tag{6}$$

The global stiffness matrix  $\mathbf{K}$  in Eq. (2) is finally assembled based on the elemental stiffness matrix  $\mathbf{K}_e$  as:

$$\mathbf{K} = \mathbf{K}_0 + \sum_{e=1}^{n_e} \mathbf{K}_e .\tag{7}$$

Here,  $\mathbf{K}_0$  is augmented to guarantee that the global stiffness matrix  $\mathbf{K}$  is symmetric positive definite, noting that for void elements, all entries of  $\mathbf{K}_e$  are zero. To minimize the influence of the augmented  $\mathbf{K}_0$  on solution accuracy, its value is assigned according to the elasticity tensor  $\mathbb{C}_0$  with  $E_0 = \varepsilon \max_m(E_m)$  and  $\nu_0 = 0.3$ , where  $\varepsilon$  is chosen to be a small value, e.g.  $10^{-4}$  in the present work. Given the assembled global stiffness matrix  $\mathbf{K}$ , the nodal displacement  $\mathbf{u}$  is obtained by solving the linear system  $\mathbf{K}\mathbf{u} = \mathbf{f}$ .

In the present work, the inequality constraint  $H_{i_H}$  is considered to be the mass constraint commonly employed in multi-material TO design, which limits the total mass of the resulting structure composed of multiple candidate materials, and is generally expressed as:

$$\begin{aligned}H_{M_0}(\boldsymbol{\rho}) &= \sum_{e=1}^{n_e} \sum_{m=1}^{n_M} \frac{\bar{M}_m}{n_e} \rho_{e,m} \leq \bar{M}_{\max} \\ H_{M_e}(\boldsymbol{\rho}) &= \sum_{m=1}^{n_M} \rho_{e,m} \leq 1, \quad e = 1, 2, \dots, n_e\end{aligned},\tag{8}$$

where  $n_M$  candidate materials has a different normalized density  $\bar{M}_m$ . The first line in the constraint denotes the global constraint for all design variables, ensuring that the total mass fraction of the resulting

structure does not exceed  $\bar{M}_{\max}$ , the maximum permissible total mass fraction. The second line imposes a local constraint that restricts each element to be occupied by at most one material. Therefore, the mass constraint in Eq. (8) essentially includes  $(1 + n_e)$  inequality constraints in total. If only a single material is involved, its normalized density is simply  $\bar{M}_1 = 1.0$ , and hence the mass constraint in Eq. (8) reduces to a volume constraint as:

$$\sum_{e=1}^{n_e} \frac{\rho_e}{n_e} \leq V_T, \quad (9)$$

which limits the total volume fraction of the single material used within the design domain  $\Omega$  to not exceed the target value  $V_T$ .

The continuum TO problem in its discrete form as in Eq. (2) is essentially a mixed integer nonlinear programming (MINLP) problem. In our prior work [20], we developed a framework based on a multi-cut formulation and adaptive trust regions for efficiently solving it, which we refer to as DVTO-MT henceforth. This framework serves as the starting point for the methodology proposed in this work. Under this framework, at each iteration step (e.g., the  $k$ -th iteration) we solve a primal problem:

$$\mathbf{u}^k = \mathbf{K}^{-1}(\boldsymbol{\rho}^k)\mathbf{f}, \quad (10)$$

and a master problem:

$$\begin{aligned} \min_{\boldsymbol{\rho}, \eta} \quad & \eta \\ \text{s.t.} \quad & \tilde{f}^j(\boldsymbol{\rho}) \leq \eta, \quad \forall j \in \mathcal{P}_s \\ & t^j(\boldsymbol{\rho}) \leq d^j, \quad \forall j \in \mathcal{P}_s \\ & H_{i_H}(\boldsymbol{\rho}) \leq 0, \quad i_H = 1, \dots, n_H \\ & \boldsymbol{\rho} \in \{0, 1\}^{n_e \times n_M}. \end{aligned} \quad (11)$$

The master problem in (11) is an optimization problem, which uses trust regions and multiple linear cuts to find the estimated upper bound  $\eta$  to the original problem (2). Each cut  $\tilde{f}^j(\boldsymbol{\rho})$ , obtained from the sensitivity analysis [13], represents a linear approximation to the original objective function as:

$$\tilde{f}^j(\boldsymbol{\rho}) = f(\mathbf{u}^j, \boldsymbol{\rho}^j) + \sum_{e=1}^{n_e} \left( \sum_{m=1}^{n_M} [\tilde{w}_{e,m}^j (\rho_{e,m} - \rho_{e,m}^j)] \right),$$

where  $\tilde{w}_{e,m}^j$  is the sensitivity of the objective function with respect to the design variable  $\rho_{e,m}$  and will be discussed with more details in the next section. The accuracy of such linear approximation is controlled by its corresponding trust region:

$$\begin{aligned} t^j(\boldsymbol{\rho}) = \frac{1}{n_M n_e} \sum_{e=1}^{n_e} \left[ \left( 1 - 2 \sum_{m=1}^{n_M} \rho_{e,m}^j \right) \left( \sum_{m=1}^{n_M} \rho_{e,m} \right) \right. \\ \left. + \left( \sum_{m=1}^{n_M} \rho_{e,m}^j \right)^2 \right] \leq d^j, \end{aligned}$$

where  $d^j$  is the radius of the trust region.

In Eq. (11),  $\mathcal{P}_s$  can include one or multiple indices  $j$  with  $j \in \{0, 1, \dots, k-1\}$ , which thereby permits leveraging the solutions and sensitivity analysis obtained in prior iteration steps to expedite the solution convergence, as discussed in our prior work [20]. If only one cut is necessary to be included, in this case

$\mathcal{P}_s = \{k - 1\}$ , the multi-cut formulation in (11) can be reduced to the following single-cut formulation:

$$\begin{aligned}
& \min_{\rho, \eta} \quad \eta \\
& \text{s.t.} \quad \tilde{f}^{k-1}(\rho) \leq \eta \\
& \quad \quad t^{k-1}(\rho) \leq d^{k-1} \\
& \quad \quad H_{i_H}(\rho) \leq 0, \quad i_H = 1, \dots, n_H \\
& \quad \quad \rho \in \{0, 1\}^{n_e \times n_M}.
\end{aligned} \tag{12}$$

A branching procedure [20] automatically determines either (11) or (12) is solved for the master problem at each iteration step. The early optimization stage typically employs (12), whereas (11) is usually invoked during the later stages for finer topology adjustments.

The primal problem (10) involves solving a large-scale linear system of equations resulting from FEM discretization, refer to as the FEM solution process. At each iteration step  $k$ , the material configuration  $\rho^k$  is fixed, and the FEM solution leads to the updated displacement field  $\mathbf{u}^k$ . The number of times the FEM solver is invoked, denoted as  $N_{\text{FEM}}$ , is equal to the total iteration count ( $N_{\text{Iter}}$ ) required to solve the original problem (2) and also the number of times the master problem (11) or (12) is solved.

The iterative process of solving the primal problem (10) and the master problem (11) or (12) yields successive upper and lower bounds for the objective function in (2). To terminate the optimization, we minimize the gap between the lowest upper bound  $U = \min_j (f(\mathbf{u}^j, \rho^j))$  for  $j \leq k$  and the lower bound  $\eta^k$  until it meets the condition  $\frac{|\eta^k - U|}{|U|} < \xi$ , with  $\xi$  being the preset tolerance and set to  $10^{-2}$  in this work.

## 2.2 Sensitivity Analysis and Filtering

The gradient of the elemental stiffness matrix  $\mathbf{K}_e$  with respect to the design variable  $\rho_{e,m}$  is calculated as:

$$\frac{\partial \mathbf{K}_e}{\partial \rho_{e,m}} = \int_{\Omega_e} \mathbf{B}^\top \frac{\partial \mathbf{C}_e}{\partial \rho_{e,m}} \mathbf{B} d\Omega = \int_{\Omega_e} \mathbf{B}^\top \mathbf{C}_m \mathbf{B} d\Omega. \tag{13}$$

To evaluate the sensitivity of the objective function with respect to the design variable  $\rho_{e,m}$ , the Lagrangian of the optimization problem is first defined as:

$$\mathbb{L}(\mathbf{u}, \rho, \boldsymbol{\mu}) = f(\mathbf{u}, \rho) + \boldsymbol{\mu}^\top [\mathbf{K}(\rho)\mathbf{u} - \mathbf{f}], \tag{14}$$

where  $\boldsymbol{\mu} \in \mathbb{R}^{3n_v}$  is the adjoint variable. According to the Karush–Kuhn–Tucker(KKT) conditions [38], the adjoint variable  $\boldsymbol{\mu}$  takes the form:

$$\boldsymbol{\mu} = -\mathbf{K}^{-1} \frac{\partial f}{\partial \mathbf{u}}, \tag{15}$$

with which, the gradient of the objective function with respect to the design variable  $\rho_{e,m}$  is calculated as:

$$\begin{aligned}
\frac{\partial f}{\partial \rho_{e,m}} &= \left( \frac{\partial f}{\partial \mathbf{u}} \right)^\top \cdot \frac{\partial \mathbf{u}}{\partial \rho_{e,m}} \\
&= \left( \frac{\partial f}{\partial \mathbf{u}} \right)^\top \frac{\partial \mathbf{K}^{-1} \mathbf{f}}{\partial \rho_{e,m}} \\
&= - \left( \frac{\partial f}{\partial \mathbf{u}} \right)^\top (\mathbf{K}^{-1})^\top \frac{\partial \mathbf{K}}{\partial \rho_{e,m}} \mathbf{K}^{-1} \mathbf{f} \\
&= - \left( \mathbf{K}^{-1} \frac{\partial f}{\partial \mathbf{u}} \right)^\top \cdot \frac{\partial \mathbf{K}}{\partial \rho_{e,m}} \mathbf{K}^{-1} \mathbf{f} \\
&= \boldsymbol{\mu}^\top \frac{\partial \mathbf{K}}{\partial \rho_{e,m}} \mathbf{u} = \boldsymbol{\mu}^\top \frac{\partial \mathbf{K}_e}{\partial \rho_{e,m}} \mathbf{u} \\
&= \boldsymbol{\mu}^\top \left( \int_{\Omega_e} \mathbf{B}^\top \mathbf{C}_m \mathbf{B} d\Omega \right) \mathbf{u}
\end{aligned} \tag{16}$$

This relation holds true whether the objective function is convex or non-convex. Finally, the sensitivity of the objective function with respect to  $\rho_{e,m}$  can be calculated as:

$$w_{e,m} = \begin{cases} \frac{\partial f}{\partial \rho_{e,m}} & \text{if } \rho_{e,m} = 1 \\ 2 \frac{\partial f}{\partial \rho_{e,m}} \cdot \frac{\partial f}{\partial \rho_{e,m'}} & \text{if } \rho_{e,m} = 0, \\ \frac{\partial f}{\partial \rho_{e,m}} + \frac{\partial f}{\partial \rho_{e,m'}} & \rho_{e,m'} = 1, m \neq m' \\ \boldsymbol{\mu}^\top \left( \int_{\Omega_e} \mathbf{B}^\top \mathbf{C}_0 \mathbf{B} d\Omega \right) \mathbf{u} & \text{if } \sum_{m=1}^{n_M} \rho_{e,m} = 0 \end{cases} \tag{17}$$

Here, while the sensitivity is directly determined as the objective function's derivative for  $\rho_{e,m} = 1$ , it needs to be regulated for  $\rho_{e,m} = 0$  [39]. Specifically, two scenarios are considered for regularization: 1) when  $\sum_{m=1}^{n_M} \rho_{e,m} = 0$ , indicating that element  $e$  is a void element, the sensitivity is calculated using the elasticity tensor  $\mathbf{C}_0$  discussed in §2.1; 2) when  $\rho_{e,m} = 0$  and  $\rho_{e,m'} = 1$  for  $m \neq m'$ , indicating element  $e$  is occupied by material  $m'$  but not  $m$ , the sensitivity is evaluated by the harmonic mean of the gradients with respect to material  $m$  and  $m'$ , respectively. The choice of harmonic mean rather than the arithmetic mean is inspired by Reuss model [40] introduced for composite material design. And our numerical experiments find that the harmonic mean is superior for selecting the optimal material in multi-material design.

Furthermore, to mitigate the so-called ‘‘checkerboard’’ artifact arising from FEM with uniform meshing [14, 41], filtering through the radius filter [15, 39] is employed to smooth the sensitivity of the objective function with respect to  $\rho_{e,m}$  as:

$$\tilde{w}_{e,m} = \frac{\sum_{e' \in \mathcal{N}_e^r} h_{e,e'}(r) w_{e,m}}{\sum_{e' \in \mathcal{N}_e^r} h_{e,e'}(r)}, \tag{18}$$

where  $h_{e,e'}(r) = \max(0, r - \|\mathbf{x}_e - \mathbf{x}_{e'}\|_2)$ ;  $e'$  denotes a neighbor element of  $e$ ; and  $r$  is the prescribed radius and set to  $3h$  in this work with  $h$  the mesh's side length.

### 3 Proposed Methodology

In the original DVTO-MT method [20], the master problems (11) or (12) are solved by directly calling a classical MILP solver, such as Gurobi [42]. While this approach is feasible for smaller 2D designs, the MILP

solver’s exponentially increasing cost can render it intractable for large-scale 3D problems, as demonstrated by our numerical tests in Sections 4.2 and 4.3.

### 3.1 Modified Dantzig-Wolfe (MDW) Decomposition

The mass constraint  $H_{M_0}(\boldsymbol{\rho}) \leq \bar{M}_{\max}$  in Eq. (8) and the cuts  $\tilde{f}^j(\boldsymbol{\rho}) \leq \eta$  and the trust regions  $t^j(\boldsymbol{\rho}) \leq d^j$  in Eq. (11) involve all design variables, and hence are categorized as *global* constraints. Whereas, the material usage constraint  $H_{M_e}(\boldsymbol{\rho}) \leq 1$  in (8) only applies to  $n_M$  variables on each element, and hence can be regarded as a *local* constraint. As a result, the programming in Eq. (11) or (12) shows a block-angular structure, and thereby can be decomposed into a series of reduced-size sub-problems through the proposed MDW decomposition. Similar to the standard DW decomposition [33], the reduced-size sub-problems are categorized as global or local, corresponding to global and local constraints, respectively. However, we cannot simply apply the standard DW decomposition, because it typically collects all extreme points, which are generated from the local sub-problems, into the global sub-problem [33]. The “extreme points” herein refer to the points satisfying the constraints of the local sub-problems. For the programming in Eq. (11) or (12) associated with the TO problems, the number of extreme points generated from each local sub-problem can scale exponentially with respect to the number of design variables involved in the local sub-problem. As the number of design variables increases, the resultant global sub-problem could become intractable. Therefore, different from the standard DW decomposition, our proposed MDW decomposition generates extreme points iteratively by updating the local sub-problems with the Lagrangian multipliers evaluated from the global sub-problem. Instead of preparing the extreme points from the local sub-problems, we search for the optimal Lagrangian multipliers as the size of Lagrangian multipliers would not scale with the number of design variables. The Lagrangian multipliers can be well initiated from a reduced-size problem (corresponding to employing a lower discretization resolution) given the TO problem is constrained by valid physical constraints, as discussed later in §3.1.3. Given the topological similarity across different discretization resolutions, only a limited number of elements need to be modified compared to the solution obtained from a lower discretization resolution, suggesting that only a small set of extreme points are required to find the optimal solution. This MDW decomposition effectively controls the size of the global sub-problem, which in turn ensures efficiency when employed to solve the master problem (11) or (12). Although proposed in the context of TO problems, this MDW decomposition is generally applicable to large-scale binary programming with non-overlapping local constraints whose size would not scale with respect to the number of variables.

The derivation uses the mass constraint in Eq. (8) as the general case, with the volume constraint in Eq. (9) treated as a special case handled similarly. To proceed, all design variables are re-indexed with:

$$\tilde{\rho}_e = \sum_{m=1}^{n_M} m \rho_{e,m}, \quad (19)$$

which assigns a new value  $\tilde{\rho}_e$  for all design variables  $\rho_{e,m}$  defined on each element  $e$ . All  $\tilde{\rho}_e$  are then sorted in a non-descending order, thereby providing each element  $e$  a new index  $e'$ . Parallel execution is possible for the sorting task, necessitating communication of the possible values for  $\tilde{\rho}_e$  among processors. Because  $\rho_{e,m}$  is binary,  $\tilde{\rho}_e$  is limited to a finite set of possible values, including  $0, 1, 2, \dots, n_M$ . This feature leads to substantial savings in communication costs, unlike general sorting algorithms that commonly require communicating sub-vectors of  $\boldsymbol{\rho}$ .

Next, with the new index  $e'$  assigned to each element, we further evenly partition all design variables into  $n_{\mathcal{D}}$  blocks with each block labeled by:

$$\mathcal{D}_i = \left\{ e \left| \left\lfloor i \cdot \frac{n_e}{n_{\mathcal{D}}} \right\rfloor \leq e' \leq \left\lfloor (i+1) \cdot \frac{n_e}{n_{\mathcal{D}}} \right\rfloor \right. \right\}. \quad (20)$$

Eq. (20) implies that the  $i$ -th block collects the indices of the elements  $e$  with the same or close value of

$\tilde{\rho}_e$ , where  $\lfloor \cdot \rfloor$  denoting the floor function. As such, each block manages about  $\frac{n_e n_M}{n_D}$  design variables. The vector  $\boldsymbol{\rho}_i$  is formed such that  $\boldsymbol{\rho}_i = \{\rho_{e,m} | \forall e \in \mathcal{D}_i, m = 1, \dots, n_M\}$ .

Following partitioning the design variables into  $n_D$  blocks, the MDW decomposition yields two types of sub-problems:  $n_D$  local sub-problems (named as they are related to the local constraint) and one global sub-problem (named as it is related to all global constraints). Each local sub-problem's size depends solely on the size of  $\mathcal{D}_i$ . In contrast, the global sub-problem's size is determined by both the number of blocks ( $n_D$ ) and the number of iterations ( $L$ ) required by the MDW decomposition, exhibiting a scaling of  $O(n_D^2 L^2)$  which is estimated from  $\sum_{l=1}^L n_D^2 l$ . However, because the number of iterations ( $L$ ) required by the MDW decomposition is independent of the number of design variables, as also evidenced in our numerical experiments, the global sub-problem's size can remain small even for large-scale TO problems.

### 3.1.1 Local and Global Sub-problem Formulations

The programming (11) involves a single continuous variable  $\eta$ . Thus, a series of variables  $\eta_i$  with  $i = 1, \dots, n_D$  are introduced to replace  $\eta$ , and thereby (11) is rewritten as:

$$\begin{aligned}
& \min_{\boldsymbol{\rho}, \boldsymbol{\eta}} \quad \sum_{i=1}^{n_D} \eta_i \\
& \text{s.t.} \quad \tilde{f}^j(\boldsymbol{\rho}) \leq \sum_{i=1}^{n_D} \eta_i, \quad \forall j \in \mathcal{P}_s \\
& \quad \quad t^j(\boldsymbol{\rho}) \leq d^j, \quad \forall j \in \mathcal{P}_s \\
& \quad \quad H_{M_0}(\boldsymbol{\rho}) \leq \bar{M}_{\max} \\
& \quad \quad \sum_{m=1}^{n_M} \rho_{e,m} \leq 1, \quad e = 1, 2, \dots, n_e \\
& \quad \quad \boldsymbol{\rho} \in \{0, 1\}^{n_e \times n_M}.
\end{aligned} \tag{21}$$

The MDW decomposition for (21) leads to  $n_D$  local sub-problems, with the  $i$ -th one ( $i = 1, 2, \dots, n_D$ ) given by:

$$\begin{aligned}
& \min_{\boldsymbol{\rho}_i, \eta_i} \quad \eta_i + \sum_{j \in \mathcal{P}_s} \pi_j^f (\tilde{f}^j(\boldsymbol{\rho}_i) - \eta_i) \\
& \quad \quad + \sum_{j \in \mathcal{P}_s} \pi_j^t t^j(\boldsymbol{\rho}_i) + \pi^M H_{M_0}(\boldsymbol{\rho}_i) \\
& \text{s.t.} \quad \sum_{m=1}^{n_M} \rho_{e,m} \leq 1, \quad e \in \mathcal{D}_i \\
& \quad \quad \boldsymbol{\rho} \in \{0, 1\}^{|\mathcal{D}_i| \times n_M}.
\end{aligned} \tag{22}$$

Given that  $\eta_i$  is unbounded,  $\sum_{j \in \mathcal{P}_s} \pi_j^f$  must be equal to 1 to guarantee a bounded objective function in (22) and in turn a feasible solution to (22). Thus, Eq. (22) can be rewritten as:

$$\begin{aligned}
& \min_{\boldsymbol{\rho}} \quad \sum_{j \in \mathcal{P}_s} \pi_j^f \tilde{f}^j(\boldsymbol{\rho}_i) + \sum_{j \in \mathcal{P}_s} \pi_j^t t^j(\boldsymbol{\rho}_i) + \pi^M H_{M_0}(\boldsymbol{\rho}_i) \\
& \text{s.t.} \quad \sum_{m=1}^{n_M} \rho_{e,m} \leq 1, \quad e \in \mathcal{D}_i \\
& \quad \quad \boldsymbol{\rho} \in \{0, 1\}^{|\mathcal{D}_i| \times n_M},
\end{aligned} \tag{23}$$

where  $\pi_j^f$ ,  $\pi_j^t$ , and  $\pi^M$  are the Lagrange multipliers obtained from solving the global sub-problem, as explained later. The local sub-problem (23) is essentially a binary programming problem. While classical computing addresses this problem with Branch and Bound (B&B)-equipped MILP solvers, its NP-complete nature suggests that quantum computing could offer a more efficient solution, as discussed later in §3.2. Further,  $n_{\mathcal{D}}$  such problems can be solved simultaneously in parallel, saving computing time and enabling an efficient parallel implementation. The solution to all local sub-problems (23) in the  $l$ -th iteration of the MDW decomposition is denoted as  $\rho_{e,m}^{k,l}$ .

The global sub-problem resulted from the MDW decomposition for (11) can then be written as:

$$\begin{aligned}
& \min_{\boldsymbol{\lambda}, \eta} \quad \eta \\
& \text{s.t.} \quad \tilde{f}^j(\bar{\boldsymbol{\rho}}) \leq \eta, \quad \forall j \in \mathcal{P}_s \\
& \quad \quad t^j(\bar{\boldsymbol{\rho}}) \leq d^j, \quad \forall j \in \mathcal{P}_s \\
& \quad \quad H_{M_0}(\bar{\boldsymbol{\rho}}) \leq \bar{M}_{\max} \\
& \quad \quad \sum_{q=1}^l \lambda_i^q = 1 \quad i = 1, 2, \dots, n_{\mathcal{D}} \\
& \quad \quad \boldsymbol{\lambda} \in [0, 1]^{n_{\mathcal{D}} \times l},
\end{aligned} \tag{24}$$

where  $\bar{\boldsymbol{\rho}} = \{\bar{\rho}_{e,m}\}$  with  $\bar{\rho}_{e,m} = \sum_{q=1}^l \rho_{e,m}^{k,l} \lambda_i^q$ ,  $\forall e \in \mathcal{D}_i, m = 1, \dots, n_M$ , and  $i = 1, 2, \dots, n_{\mathcal{D}}$ . It is a linear programming problem, with both  $\boldsymbol{\lambda}$  and  $\eta$  continuous variables, and can be easily solved by a classical linear programming solver, e.g., Gurobi Optimizer [42] used in this work. During the solution of the global sub-problem (24), the Lagrange multipliers  $\pi_j^f$ ,  $\pi_j^t$ , and  $\pi^M$  are determined concurrently with  $\boldsymbol{\lambda}$  and  $\eta$  by the linear programming solver. These Lagrange multipliers correspond to the conversion of the three inequality constraints in (24) into equality constraints and are collectively denoted as the vector  $\boldsymbol{\pi}$ .

Similarly, the programming (12) can be written as

$$\begin{aligned}
& \min_{\boldsymbol{\rho}} \quad \sum_{e=1}^{n_e} \sum_{m=1}^{n_M} \tilde{w}_{e,m}^{k-1} \rho_{e,m} \\
& \text{s.t.} \quad t^{k-1}(\boldsymbol{\rho}) \leq d^{k-1} \\
& \quad \quad \sum_{e=1}^{n_e} \sum_{m=1}^{n_M} \frac{\bar{M}_m}{n_e} \rho_{e,m} \leq \bar{M}_{\max} \\
& \quad \quad \sum_{m=1}^{n_M} \rho_{e,m} \leq 1, \quad e = 1, 2, \dots, n_e \\
& \quad \quad \boldsymbol{\rho} \in \{0, 1\}^{n_e \times n_M}.
\end{aligned} \tag{25}$$

Applying the MDW decomposition to (25), the resultant  $i$ -th local sub-problem is given by:

$$\begin{aligned}
& \min_{\boldsymbol{\rho}_i} \quad \sum_{e \in \mathcal{D}_i} \sum_{m=1}^{n_M} \tilde{w}_{e,m}^{k-1} \rho_{e,m} + \pi^t t^{k-1}(\boldsymbol{\rho}_i) + \pi^M H_{M_0}(\boldsymbol{\rho}_i) \\
& \text{s.t.} \quad \sum_{m=1}^{n_M} \rho_{e,m} \leq 1, \quad e \in \mathcal{D}_i \\
& \quad \quad \boldsymbol{\rho}_i \in \{0, 1\}^{|\mathcal{D}_i| \times n_M},
\end{aligned} \tag{26}$$

and the corresponding global sub-problem reads:

$$\begin{aligned}
\min_{\lambda} \quad & \sum_{e=1}^{n_e} \left( \sum_{m=1}^{n_M} [\tilde{w}_{e,m}^{k-1} (\bar{\rho}_{e,m} - \rho_{e,m}^{k-1})] \right) \\
\text{s.t.} \quad & t^{k-1}(\bar{\rho}) \leq d^{k-1} \\
& \sum_{e=1}^{n_e} \sum_{m=1}^{n_M} \frac{\bar{M}_m}{n_e} \bar{\rho}_{e,m} \leq \bar{M}_{\max} \\
& \sum_{q=1}^l \lambda_i^q = 1, \quad i = 1, 2, \dots, n_{\mathcal{D}} \\
& \lambda \in [0, 1]^{n_{\mathcal{D}} \times l}.
\end{aligned} \tag{27}$$

Like (23), (26) is a binary programming problem, while (27) is a linear programming problem, similar to (24).

### 3.1.2 Initialization

To initiate the MDW decomposition, an initial guess of  $\rho$  to the programming (11) or (12) is necessary. Thus, we propose solving a reduced-size problem with a clustered design variable  $\hat{\rho} \in \{0, 1\}^{n_{\mathcal{D}} \times n_M}$  to obtain the initial guess. Specifically, we assign all design variables  $\rho_{e,m}$  in the  $i$ -th block with a single value of  $\hat{\rho}_{i,m}$ , i.e.,  $\rho_{e,m} = \hat{\rho}_{i,m}$ ,  $\forall e \in \mathcal{D}_i$ . As such, the design variables  $\rho_{e,m}$  belong to the  $i$ -th block are aggregated into one variable  $\hat{\rho}_{i,m}$ , and correspondingly the coefficients associated with the design variables in (11) or (12) are also aggregated. The resultant reduced-size multi-cut problem reads:

$$\begin{aligned}
\min_{\hat{\rho}, \eta} \quad & \eta \\
\text{s.t.} \quad & f(\rho^j, \mathbf{u}^j) + \sum_{m=1}^{n_M} \sum_{i=1}^{n_{\mathcal{D}}} \left( \sum_{e \in \mathcal{D}_i} \tilde{w}_{e,m}^j \right) \hat{\rho}_{i,m} \\
& - \sum_{e=1}^{n_e} \sum_{m=1}^{n_M} \tilde{w}_{e,m}^j \rho_{e,m}^j \leq \eta, \quad \forall j \in \mathcal{P}_s \\
& \frac{1}{n_e} \sum_{m=1}^{n_M} \sum_{i=1}^{n_{\mathcal{D}}} \left[ \sum_{e \in \mathcal{D}_i} \left( 1 - 2 \sum_{m=1}^{n_M} \rho_{e,m}^j \right) \right] \hat{\rho}_{i,m} \\
& + \sum_{e=1}^{n_e} (\rho_{e,m}^j)^2 \leq d^j, \quad \forall j \in \mathcal{P}_s \\
& \sum_{m=1}^{n_M} \sum_{i=1}^{n_{\mathcal{D}}} \frac{\bar{M}_m \cdot |\mathcal{D}_i|}{n_e} \hat{\rho}_{i,m} \leq \bar{M}_{\max} \\
& \sum_{m=1}^{n_M} \hat{\rho}_{i,m} \leq 1, \quad i = 1, 2, \dots, n_{\mathcal{D}} \\
& \hat{\rho} \in \{0, 1\}^{n_{\mathcal{D}} \times n_M}.
\end{aligned} \tag{28}$$

And the resultant reduced-size single-cut problem is given by:

$$\begin{aligned}
\min_{\hat{\rho}} \quad & \sum_{m=1}^{n_M} \sum_{i=1}^{n_{\mathcal{D}}} \left( \sum_{e \in \mathcal{D}_i} \tilde{w}_{e,m}^{k-1} \right) \hat{\rho}_{i,m} \\
\text{s.t.} \quad & \frac{1}{n_e} \sum_{m=1}^{n_M} \sum_{i=1}^{n_{\mathcal{D}}} \left[ \sum_{e \in \mathcal{D}_i} \left( 1 - 2 \sum_{m=1}^{n_M} \rho_{e,m}^{k-1} \right) \right] \hat{\rho}_{i,m} \\
& + \sum_{e=1}^{n_e} (\rho_{e,m}^{k-1})^2 \leq d^{k-1} \\
& \sum_{m=1}^{n_M} \sum_{i=1}^{n_{\mathcal{D}}} \frac{\bar{M}_m \cdot |\mathcal{D}_i|}{n_e} \hat{\rho}_{i,m} \leq \bar{M}_{\max} \\
& \sum_{m=1}^{n_M} \hat{\rho}_{i,m} \leq 1, \quad i = 1, 2, \dots, n_{\mathcal{D}} \\
& \hat{\rho} \in \{0, 1\}^{n_{\mathcal{D}} \times n_M}.
\end{aligned} \tag{29}$$

Both can be solved by a standard MILP solver. In case that the initialization problem (28) or (29) is infeasible,  $n_{\mathcal{D}}$  will be doubled, and (28) or (29) will then be reformulated with the new  $n_{\mathcal{D}}$ . This process can be repeated until a feasible solution to the initialization problem is found. Our numerical experiments indicate that infeasible solutions are uncommon during the initialization stage, provided  $n_{\mathcal{D}}$  is not set too small. For all numerical experiments in this work, we set  $n_{\mathcal{D}} = 100$ . The solution to the initialization problem yields the initial Lagrange multiplier values, which are then used when solving the local sub-problems in the first iteration step.

Since the size of the clustered design variable  $\hat{\rho}$  depends only on the number of blocks ( $n_{\mathcal{D}}$ ) and the number of materials ( $n_M$ ), the initialization cost stays low, even when tackling large-scale TO problems.

### 3.1.3 Iteration Process and Algorithm

The iteration process of the MDW decomposition starts with the initialization step of solving the reduced-size problem (28) or (29). Then at each iteration step  $l$ , the  $n_{\mathcal{D}}$  local sub-problems (23) or (26) are solved to yield  $\rho_{e,m}^{k,l}$ , with the Lagrangian multipliers obtained from solving the global sub-problem (24) or (27) in the last iteration. The design variables  $\rho_{e,m}$  in the original programming (11) or (12) are finally updated by the design variables  $\rho_{e,m}^{k,L}$  at the end of the iteration process of MDW.

The iteration process is terminated once the convergence criterion is satisfied, which is defined by the Lagrange multipliers  $\boldsymbol{\pi}$  obtained from the global sub-problem, as:

$$\frac{\|\boldsymbol{\pi}^l - \boldsymbol{\pi}^{l-1}\|_2}{\|\boldsymbol{\pi}^{l-1}\|_2} \leq 10^{-6}. \tag{30}$$

Here, the vector  $\boldsymbol{\pi}$  is defined as:  $\boldsymbol{\pi} = \{\pi^f, \pi^t, \pi^M\}$  if the original programming is multi-cut as in (11), or  $\boldsymbol{\pi} = \{\pi^t, \pi^M\}$  if the original programming is single-cut as in (12).

The entire process for the proposed MDW decomposition, including its initiation and iteration process, is summarized in Algorithm 1.

---

**Algorithm 1** MDW DECOMPOSITION

---

**Input:** Programming (11) or (12) and the value of  $n_{\mathcal{D}}$

**Output:** The optimal solution  $\rho$  and the objective function value  $\eta$  to the programming (11) or (12)

**Utility:** Use MDW decomposition to solve the programming (11) or (12)

- 1: Calculate  $\tilde{\rho}$  according to (19) and sort  $\tilde{\rho}$  in non-descending order
  - 2: Partition the design variables into  $n_{\mathcal{D}}$  blocks according to (20)
  - 3: Solve the initialization problem (28) or (29)
  - 4: **if** (28) or (29) is infeasible **then**
  - 5:      $n_{\mathcal{D}} = 2 \cdot n_{\mathcal{D}}$
  - 6:     Go to Step 2
  - 7: **else**
  - 8:     Update the design variables  $\rho_{e,m}^{k,0}$  with the solution of the initialization problem and update the corresponding Lagrange multipliers  $\pi^0$
  - 9: **end if**
  - 10: **for**  $l = 1, 2, \dots$  **do**
  - 11:     Solve all  $n_{\mathcal{D}}$  local sub-problems (23) or (26)
  - 12:     Update the design variables  $\rho_{e,m}^{k,l}$
  - 13:     Solve the global sub-problem (24) or (27) and update the corresponding Lagrange multipliers  $\pi^l$
  - 14:     **if**  $\frac{\|\pi^l - \pi^{l-1}\|_2}{\|\pi^{l-1}\|_2} \leq 10^{-6}$  **then**
  - 15:         **Break**
  - 16:     **end if**
  - 17: **end for**
- Return:**  $\rho^{k,l}, \eta$
- 

## 3.2 Quantum Implementation

A QUBO problem generally reads:

$$\begin{aligned} \mathbb{Z}^* &= \min_{\mathbb{Z} \in \{0,1\}^n} \mathcal{J} \\ \mathcal{J} = \mathbb{Z}^\top \mathbf{Q} \mathbb{Z} &= \sum_{i=1}^n Q_{ii} \mathbb{Z}_i + \sum_{i=1}^n \sum_{j=i+1}^n Q_{ij} \mathbb{Z}_i \mathbb{Z}_j, \end{aligned} \quad (31)$$

where  $\mathbb{Z}$  denotes a binary variable, and  $\mathbf{Q}$  represents the coefficient matrix. Directly converting the MILP problem (11) or (12) into an equivalent QUBO problem presents a significant hurdle. This is because when the global constraints that involve all design variables are incorporated into the objective function  $\mathcal{J}$  (e.g., through a penalty method), they can lead to a dense coefficient matrix  $\mathbf{Q}$ . A dense  $\mathbf{Q}$  matrix has two major implications. First, solving the resulting QUBO problem necessitates an all-to-all connection between qubits, which is a demanding requirement for current quantum hardware. Second, the computational cost of constructing the  $\mathbf{Q}$  matrix itself scales quadratically with the number of design variables (i.e.,  $n_e \times n_M$ ). This substantial classical pre-computation effectively negates any potential quantum speedup, making the overall approach inefficient.

The proposed MDW decomposition introduced in §3.1 provides a systematic way to decompose the MILP problems like (11) or (12) into a series of two types of sub-problems: Binary Programming (or Binary Integer Programming, BIP) (23) or (26); and Linear Programming (LP) (24) or (27). Thereby, we solve totally  $n_{\mathcal{D}}$  BIP problems and one LP problem in each iteration step of the MDW decomposition. The LP problem can be easily solved by invoking an off-the-shelf classical LP solver, e.g., provided by Gurobi [42]. The overall computational cost is then dominated by solving  $n_{\mathcal{D}}$  BIP problems. Compared to classical optimizers,

quantum computing is known to be more efficient for solving BIP problems. For example, by leveraging the “quantum tunneling” effect, quantum annealing can pass through high energy peaks without requiring to follow the energy landscape, and hence effectively avoid falling into local minimum. As a result, it can find the global minimum (the lowest energy state) significantly faster. Therefore, this section focuses on the quantum implementation for solving the BIP problems (23) and (26).

To proceed, we formulate each problem into the form of QUBO. First, the binary constraints in both problems are the same and can be converted into the QUBO form as:

$$\sum_{e \in \mathcal{D}_i} \left[ \sum_{m=1}^{n_M} \rho_{e,m} + \phi_e - 1 \right]^2, \quad (32)$$

where  $\phi_e$  is a slackness variable introduced for restricting the material usage on each element  $e$ .

Second, as the objective function is linear for both problems, the QUBO formed for each problem (23) or (26) requires only  $(n_M + 1) \times |\mathcal{D}_i|$  logical qubits. While the QUBO for the multi-cut BIP problem (23) is given by:

$$\begin{aligned} & \sum_{e \in \mathcal{D}_i} \sum_{j \in \mathcal{P}_s} \pi_j^f \tilde{f}^j(\boldsymbol{\rho}_i) + \sum_{j \in \mathcal{P}_s} \pi_j^t t^j(\boldsymbol{\rho}_i) + \pi^M H_{M_0}(\boldsymbol{\rho}_i) \\ & + \Pi \sum_{e \in \mathcal{D}_i} \left[ \sum_{m=1}^{n_M} \rho_{e,m} + \phi_e - 1 \right]^2, \end{aligned} \quad (33)$$

the QUBO for the single-cut BIP problem (26) can be written as:

$$\begin{aligned} & \sum_{e \in \mathcal{D}_i} \sum_{m=1}^{n_M} \tilde{w}_{e,m}^{k-1} \rho_{e,m} + \pi^t t^{k-1}(\boldsymbol{\rho}_i) + \pi^M H_{M_0}(\boldsymbol{\rho}_i) \\ & + \Pi \sum_{e \in \mathcal{D}_i} \left[ \sum_{m=1}^{n_M} \rho_{e,m} + \phi_e - 1 \right]^2. \end{aligned} \quad (34)$$

Here,  $\Pi$  in either of the above two equations is a large positive constant to penalize the binary constraint. As  $\tilde{f}^j$  in the cuts,  $t^j$  for the trust regions, and the total mass  $H_{M_0}$  are all bounded with respect to the design variables  $\boldsymbol{\rho}$ ,  $\Pi$  can be straightforwardly set to their upper bounds as:

$$\Pi = \max \left( \pi_j^f \sum_{e \in \mathcal{D}_i} \sum_{m=1}^{n_M} |\tilde{w}_{e,m}^j|, \pi_j^t d^j, \pi^M \bar{M}_{\max} \right) \quad (35)$$

for (23) and

$$\Pi = \max \left( \sum_{e \in \mathcal{D}_i} \sum_{m=1}^{n_M} |\tilde{w}_{e,m}^{k-1}|, \pi^t d^{k-1}, \pi^M \bar{M}_{\max} \right) \quad (36)$$

for (26). Here,  $\sum_{e \in \mathcal{D}_i} \sum_{m=1}^{n_M} |\tilde{w}_{e,m}^j|$  is used as the upper bound of  $\tilde{f}^j(\boldsymbol{\rho}_i)$ .

## 4 Results

The proposed method is evaluated for its solution quality and computational efficiency through large-scale 3D bridge design problems, including both single and multi-material cases. Robustness and scalability are assessed by varying the discretization resolution, with the largest design comprising over 10 million discrete

elements and more than 50 million design variables. Comparative analyses against representative classical methods, including SIMP [19] and DVTO-MT [20], demonstrate the superior performance of our new method.

The FEM solver used in this work is FEniCSx [43], which is based on FEniTop [19], a parallel scalable implementation that employs FEniCSx for solving TO problems.

## 4.1 Problem Setup

The design domain is a 3D box, with the length of  $L = 40$  m, the width of  $W = 10$  m, and the height of  $H = 10$  m, as depicted in Figure 1. A solid plate with the thickness of 0.4 m is placed on top of the box, designated by the red region in Figure 1. This top plate region is excluded from the TO design, and hence is always assigned solid elements of the strongest material. The design domain is fixed in two striped regions at either end of the bottom boundary, each with a width of 2 m, as designated by the orange regions in Figure 1. The gray region represents the actual design domain, allowing for free-form topologies and the use of any candidate materials, as determined by the optimization solution. A uniformly distributed loading force with the magnitude of  $-10^3 N/m^2$  is exerted on the top boundary of the design domain, as indicated by blue arrows in Figure 1. Three different discretization resolutions are examined, including  $50 \times 200 \times 50$ ,  $100 \times 400 \times 100$ , and  $150 \times 600 \times 150$ .

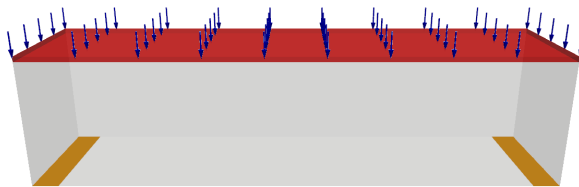


Figure 1: Domain setup and boundary conditions for 3D bridge design.

For the single-material design scenario, the material considered is stainless steel. Whereas, for multi-material TO designs, we include four representative metallic materials, whose mechanical properties are detailed in Table 1. These materials, magnesium, aluminum, titanium, and stainless steel, represent a selection of the most widely utilized metallic materials in structural engineering applications. They also span a range of properties, including Young’s modulus, Poisson’s ratio, and density. The inclusion of diverse materials allows us to demonstrate the proposed method’s capability to autonomously select optimal materials during optimization. For the multi-material design, we set the maximum total mass to  $3.744 \times 10^6$  kg. This value is equivalent to a 12% volume fraction if only steel were used in the single-material design. Given that the top plate of the design domain consistently uses steel across all scenarios, the mass of material actually subject to optimization is reduced to  $2.496 \times 10^6$  kg for the multi-material design, which corresponds to an 8% volume fraction when only using steel for the single-material design. The design objective is to minimize the compliance of the bridge, i.e., in Eq. (2),  $f(\mathbf{u}, \boldsymbol{\rho}) = \mathbf{f}^\top \mathbf{u}$ . With this design, the bridge’s topology and usage of candidate material(s) are optimized to withstand the applied external load.

## 4.2 Single-Material Design

For the single-material design,  $n_M = 1$ , and as mentioned above, stainless steel is the material used for the design. The results obtained from three different methods are compared, including the proposed MDW decomposition method in this work, the SIMP method [19], and the original DVTO-MT method [20]. In light of current quantum hardware access limitations, we validate our proposed MDW decomposition method through a two-tiered approach. The first tier involves validating its classical implementation by solving local

Table 1: Properties of the four candidate materials considered in multi-material TO design.

Materials	Magnesium	Aluminum	Titanium	Stainless steel
Young’s modulus $E_m$ (GPa)	44	73	100	210
Poisson’s ratio $\nu_m$	0.28	0.33	0.36	0.29
Mass density $\bar{M}_m$ ( $10^3 \times \text{kg/m}^3$ )	1.74	2.70	4.50	7.80
Specific strength $\frac{E_m}{\bar{M}_m}$ ( $10^6 \times \frac{\text{N}\cdot\text{m}}{\text{kg}}$ )	25.3	27.0	22.2	26.9

sub-problems (23) or (26) with a classical optimizer provided by Gurobi [42]. The corresponding results are referred to as “**MDW-CC**”. In the second tier, we validate the QUBO formulation for the multi-cut BIP problem (23) by solving it using the QAOA algorithm.

For the first-tier validation, we begin with comparing the results with those of SIMP. Table 2 summarizes the results for the optimal objective function value ( $f$ ), the total iteration count ( $N_{\text{Iter}}$ ), and the total computing time ( $T_{\text{tot}}$ , at different discretization resolutions. The total iteration count for solving the TO problem (2) dictates the number of FEM solver calls, making it a key indicator of methodological efficiency, alongside computing time. For the SIMP results, we adopted a recent scalable implementation, *FEniTop* [19], used the optimality criterion (OC) for its optimal performance, and set the maximum number of iterations to 400 and the Helmholtz filter radius to 0.6. By comparing the objective function values, we find that the SIMP method requires at least 400 iterations to achieve comparably low values; terminating earlier, such as at 200 iteration steps, does not yield sufficiently low objective function values. This significantly higher iteration count results in far more frequent FEM solution invocations and a greatly increased number of optimization problem solutions. This, in turn, leads to much longer total computing times for SIMP, almost an order of magnitude greater than our method’s classical implementation (MDW-CC). Moreover, since the  $n_D$  local sub-problems can be solved independently, our implementation solves them in parallel during each MDW iteration. All computing times reported herein are wall times measured on a single node equipped with two AMD EPYC 7763 64-Core Processors and 512 GB of memory. Each test was launched via the Slurm system [44], utilizing all 128 physical cores of the node.

Table 2: Single-material design: The resultant objective function value ( $f$ ), total iteration count ( $N_{\text{Iter}}$ ), and total computing time ( $T_{\text{tot}}$ ), compared with the SIMP method [19].

Resolution	MDW-CC			SIMP ( $N_{\text{Iter}} = 200$ )			SIMP ( $N_{\text{Iter}} = 400$ )		
	$f$	$N_{\text{Iter}}$	$T_{\text{tot}}$ (s)	$f$	$\Delta f$ (%)	$T_{\text{tot}}$ (s)	$f$	$\Delta f$ (%)	$T_{\text{tot}}$ (s)
$50 \times 200 \times 50$	15.229	77	370.9	19.172	25.9	1015.4	16.148	6.0	2821.8
$100 \times 400 \times 100$	14.115	67	2445.7	18.418	30.5	9235.7	14.499	2.7	20261.4
$150 \times 600 \times 150$	13.205	47	6434.2	18.231	38.1	37004.4	14.048	6.4	84163.0

Next, we compare the resultant optimal topologies. The ones obtained by MDW-CC are shown in Figure 2 at varying discretization resolutions. Our method can generate clear-cut 0/1 topologies, because it directly uses binary design variables. As the discretization is refined, the optimal topology reveals finer structures and develops more branches under the top plate. The optimal topologies obtained by the SIMP method are reported in Figure 3. Since SIMP does not produce clear-cut topologies, the results in Figure 3 are shown after a post-processing filter with the threshold of 0.5, by which the design variable  $\rho$  ranges continuously from 0.5 to 1, as depicted by varied colors in Figure 3. Comparing the left half (presenting the outcome after 200 iteration steps) and the right half (after 400 iteration steps), it is evident that SIMP needs more iterations to reach not only lower objective function values (as indicated in Table 2) but also further evolving

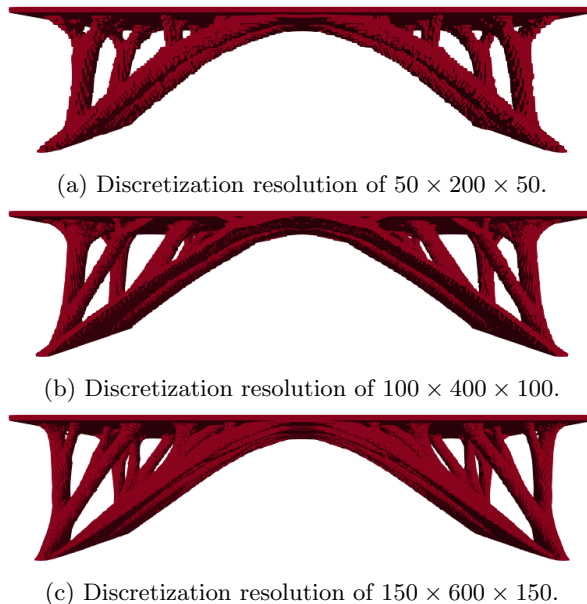


Figure 2: Single-material design: The optimal topologies yield by our method with three discretization resolutions.

topologies.

Further comparison with the original DVTO-MT method [20] focuses solely on the total time dedicated to solving master problems, denoted as  $T_{\text{OPT}}$ , because MDW also adheres to the DVTO-MT framework, solving the same primal problem and employing the same parameter relaxation scheme, thus requiring the same total iteration counts ( $N_{\text{Iter}}$ ) and FEM solution time ( $T_{\text{FEM}}$ ) as the original DVTO-MT method [20]. This comparison, detailed in Table 3, elucidates the superior efficiency of MDW compared to employing a MILP solver [42] for master problems (11) or (12). The optimization time incurred by the MILP solver is comparable to FEM solution time, making the solution of large-scale TO problems very expensive. In contrast, our MDW method achieves substantial speedup, reaching more than an order of magnitude. This speedup becomes more pronounced with increasing problem size, establishing MDW as a practically efficient approach for 3D large-scale TO problems. For multi-material designs, the speedup proves even more significant, a point elaborated later in §4.3.

Table 3: Single-material design: The time spent for optimization ( $T_{\text{OPT}}$ ), compared with the original DVTO-MT method [20]. Here, the FEM solution time ( $T_{\text{FEM}}$ ) is provided for reference.

Resolution	$T_{\text{FEM}}$ (s)	$T_{\text{OPT}}^{\text{MDW-CC}}$ (s)	$T_{\text{OPT}}^{\text{DVTO-MT}}$ (s)	$T_{\text{OPT}}^{\text{DVTO-MT}}/T_{\text{OPT}}^{\text{MDW-CC}}$
$50 \times 200 \times 50$	303.3	67.6	268.1	4.0
$100 \times 400 \times 100$	2282.2	163.5	2824.8	17.3
$150 \times 600 \times 150$	6234.0	200.2	5254.6	26.2

As discussed in §3.2, the local sub-problems (22) or (26) can be solved using quantum computing to leverage its advantages in solving BIP problems. Thus, in the second-tier validation, we verify the QUBO formulated for the local sub-problems. Due to the practical limitations of accessing real quantum hardware, we opted to solve the QUBO in (33) with the QAOA algorithm, leveraging the simulator provided by

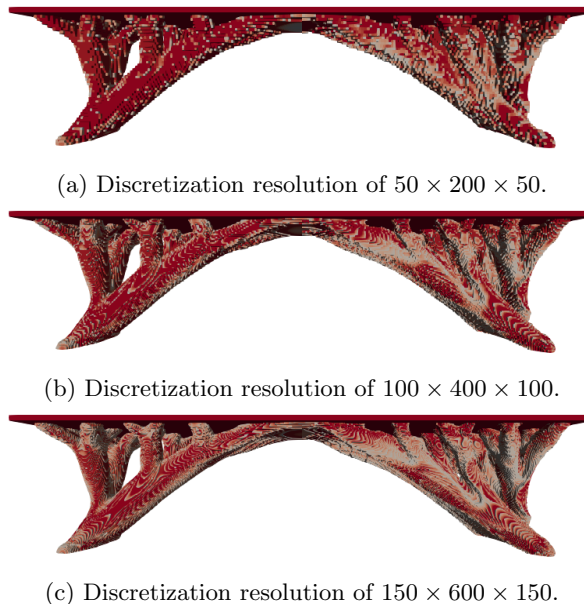


Figure 3: Single-material design: The optimal topologies produced by the SIMP method with three discretization resolutions. For each topology, the left half presents the outcome after 200 iteration steps, and the right half after 400 iteration steps. The color intensity reflects the values of the design variable  $\rho$  following a post-processing filter with the threshold of 0.5, where darker shades indicate values closer to 1 and lighter shades represent values closer to 0.5.

cuda-quantum [45]. Given the limited number of qubits that can be simulated on a classical computer, we constrained the size of  $|\mathcal{D}_i|$  up to 8 for validation purposes. Thirty local sub-problems were randomly selected from the case with the discretization resolution of  $50 \times 200 \times 50$ . The number of layers in the ansatz was set to  $\mathcal{L} = 4$  or  $\mathcal{L} = 5$ . To evaluate accuracy, we compared the QUBO’s solution generated by QAOA against that yield by calling the classical optimizer [42] for solving the original local sub-problem. The accuracy is evaluated by the percentage of agreement between the two solutions across all 30 problems solved, as presented in Table 4. The results show that with a sufficient number of layers in the ansatz, specifically  $\mathcal{L} = 5$ , our QUBO formulation successfully guides the optimization to the desired solution, thus validating its use for updating design variables in the TO process.

Table 4: Validation of QUBO: (33) solved by QAOA for 30 randomly selected local sub-problems. Here, the accuracy is evaluated by the percentage of agreement with the solutions yield by calling the classical optimizer [42] for solving (23);  $\mathcal{L}$  denotes the number of layers in the ansatz; and  $|\mathcal{D}_i|$  is the sub-problem’s size.

$\mathcal{L} = 4$						
$ \mathcal{D}_i $	3	4	5	6	7	8
Accuracy	100%	100%	100%	98.3%	94.3%	64.2%
$\mathcal{L} = 5$						
$ \mathcal{D}_i $	3	4	5	6	7	8
Accuracy	100%	100%	100%	100%	100%	95.4%

Finally, we assess the potential quantum speedup. As previously mentioned, quantum computing can accelerate the solution of local sub-problems, which is the dominant cost in solving the master problem (11) or (12) via MDW. Although we cannot access actual quantum hardware to solve them, we can estimate the computing time and potential quantum speedup. The expected computing time on a QPU, when quantum annealers [32] are used to solve the QUBO in (33), can be estimated as:

$$T_{\text{QPU}} = 20\mu\text{s} \times 1000 \times N_{\text{Local}} , \quad (37)$$

where  $T_{\text{QPU}}$  denotes the expected total QPU time for 1000 repetitions of annealing, with each annealing process taking  $20\mu\text{s}$  [32]; and  $N_{\text{Local}} = N_{\text{Iter}} \times L$  is the total number of local sub-problems involved in the entire solution process, which can be evaluated from our classical implementation of MDW. The embedding overhead on the QPU is excluded from this estimation. This is because embedding time is difficult to estimate, varies significantly with hardware, and, more importantly, a key advantage of the proposed MDW decomposition is that the resulting QUBOs (33) or (34) do not require all-to-all qubit connections, thus avoiding long embedding times. It should also be noted that, since the  $n_D$  local sub-problems can be solved independently in each MDW iteration and were solved in parallel in our classical implementation, for a fair comparison, we assume that the quantum hardware accessed can simultaneously solve the corresponding  $n_D$  QUBO problems. Such estimated time is presented in Table 5. In addition to the QPU time, the actual cost of solving the QUBO must also account for the time spent on forming the QUBO (33) or (34), denoted as  $T_{\text{QUBO}}$ . This step, performed on a classical computer, was implemented with its wall time measured and reported in Table 5. Thus, the potential quantum speedup factor is estimated from:

$$\text{Speedup} = \frac{T_{\text{Local}}^{\text{MDW-CC}}}{T_{\text{QPU}} + T_{\text{QUBO}}} , \quad (38)$$

where  $T_{\text{Local}}^{\text{MDW-CC}}$  denotes the total wall time incurred by using the classical optimizer to solve all local sub-problems. The speedup, as shown in Table 5, becomes more pronounced with larger problem sizes. This speedup can be more significant for multi-material designs, a point discussed further in §4.3.

Table 5: Single-material design: Quantum computing time estimated and potential speedup.

<b>Resolution</b>	$N_{\text{Local}}$	$T_{\text{QPU}}$ (s)	$T_{\text{QUBO}}$ (s)	$T_{\text{Local}}^{\text{MDW-CC}}$ (s)	Speedup
$50 \times 200 \times 50$	1039	20.8	0.1	29.0	1.4
$100 \times 400 \times 100$	1444	28.9	1.5	90.3	3.0
$150 \times 600 \times 150$	699	14.0	1.7	137.8	8.8

### 4.3 Multi-Material Design

For the multi-material design, all four candidate materials in Table 1 are involved. The design goal is twofold: optimizing the bridge’s structural topology and selecting the optimal material combination, as shown in Figure 4. Among the four candidate materials, only three were selected in the final design: titanium was excluded. This is because titanium’s significantly lower specific strength ( $E_m/\bar{M}_m$ ) makes it less efficient for minimizing compliance while maintaining a lightweight structure. The other three materials have comparable specific strengths, but stainless steel, despite its high Young’s modulus, has the greatest mass density. As a result, it forms the smallest fraction of the final material selection, primarily used for parts near the center beneath the plate and close to the two bottom supports where maximum stiffness is needed. Both magnesium and aluminum are lightweight and thus dominate the final material selection. Magnesium, being the softest, appears mostly as the outer coating, while aluminum serves as an intermediate, transitional

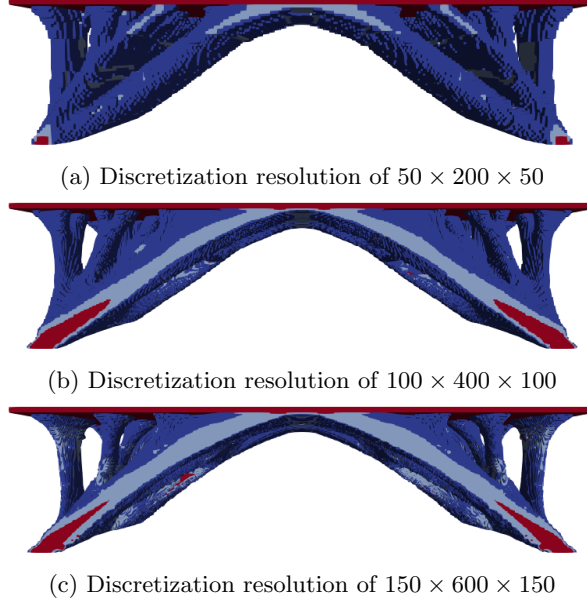


Figure 4: Multi-material design: The optimal topologies and material selections obtained from our method at three discretization resolutions. Materials are rendered as follows: Magnesium (dark blue), Aluminum (light blue), Titanium (orange), and Stainless Steel (red).

material between magnesium and stainless steel. This alignment with intuitive material selection principles supports our method’s ability to correctly identify optimal materials.

Since the SIMP method [19] cannot account for multiple materials, we only compare our method with the original DVTO-MT method [20] herein. Similar to the single-material design, our comparison with the original DVTO-MT method [20] focuses solely on  $T_{\text{OPT}}$ , the total time dedicated to solving master problems (11) or (12), as detailed in Table 6. While both methods maintain the low iteration counts and comparable FEM solution time as observed in the single-material case, the multi-material design involves four times the number of design variables. This increase of design variables escalates the time spent solving the master problems compared to the single-material scenario. Notably, MDW’s cost increases only slightly, whereas the MILP solver’s cost rises exponentially, causing its optimization time to even exceed the FEM solution time by orders of magnitude. For the case of  $100 \times 400 \times 100$ , our method achieves a remarkable speedup by three orders of magnitude. Furthermore, for the largest problem ( $150 \times 600 \times 150$ , resulting in 54 million design variables), the MILP solver fails to provide a solution, yet MDW’s time remains less than the FEM solution time, further substantiating its superior efficiency and practical utility for tackling large-scale 3D TO problems.

Table 6: Multi-material design: The resultant objective function value ( $f$ ), total iteration count ( $N_{\text{Iter}}$ ), and the FEM solution time ( $T_{\text{FEM}}$ ). The time spent for optimization ( $T_{\text{OPT}}$ ) is compared with the original DVTO-MT method [20].

Resolution	$f$	$N_{\text{Iter}}$	$T_{\text{FEM}}$ (s)	$T_{\text{OPT}}^{\text{MDW-CC}}$ (s)	$T_{\text{OPT}}^{\text{DVTO-MT}}$ (s)	$T_{\text{OPT}}^{\text{DVTO-MT}}/T_{\text{OPT}}^{\text{MDW-CC}}$
$50 \times 200 \times 50$	12.957	39	123.6	61.1	6118.6	100
$100 \times 400 \times 100$	13.052	44	1746.6	285.2	349929.0	1227
$150 \times 600 \times 150$	12.983	51	9667.1	2089.3	–	–

The assessment of potential quantum speedup for multi-material designs follows the same approach as in the single-material cases. Table 7 summarizes the estimated speedup. We observe that the speedup becomes increasingly pronounced as the problem size grows. For the largest test case, with a discretization resolution of  $150 \times 600 \times 150$ , the observed rise in  $T_{\text{QUBO}}$ , i.e., the time required to construct the QUBO, primarily results from an inefficient Python implementation relying on nested loops. This bottleneck can be substantially mitigated through more efficient coding practices, such as vectorizing the Python implementation or transitioning to a compiled language like C++. Such improvements are expected to substantially enhance the scalability of  $T_{\text{QUBO}}$  and greatly reduce it for larger problems. This will, in turn, make the quantum speedup even more pronounced with increasing problem sizes. It is also worth noting that quantum advantage is significantly greater for multi-material designs compared to single-material designs. Thus, we anticipate that quantum computing will become increasingly impactful as the complexity and scale of TO designs continue to grow in real-world applications.

Table 7: Multi-material design: Quantum computing time estimated and potential speedup.

<b>Resolution</b>	$N_{\text{Local}}$	$T_{\text{QPU}}$ (s)	$T_{\text{QUBO}}$ (s)	$T_{\text{Local}}^{\text{MDW-CC}}$ (s)	Speedup
$50 \times 200 \times 50$	659	13.2	0.3	30.3	2.3
$100 \times 400 \times 100$	756	15.1	2.2	224.7	13.0
$150 \times 600 \times 150$	1400	28.0	29.7	1626.1	28.2

## 5 Conclusion

We have presented a new methodology capable of efficiently solving TO problems while enabling the integration of quantum computing to harness potential quantum advantages. This work has targeted on addressing large-scale, multi-material TO challenges for 3D continuum structures, representing a significant departure from previous research that leveraged quantum computing in TO [21, 34–36, 46]. Those studies primarily tackled discrete truss structures or linear or small-scale continuum problems, overlooked the additional cost induced by constructing QUBO, and exclusively dealt with single-material designs. At the heart of this new methodology is the MDW decomposition, which effectively addresses the escalating computational cost associated with using classical MILP solvers to directly solve the master problems in the DVTO-MT framework [20] that features a multi-cut formulation and adaptive trust regions and can significantly reduce iteration counts, and in turn, the time required for solving the governing PDE via FEM. The MDW decomposition breaks down each MILP problem into  $n_D$  local sub-problems (BIP) and one global sub-problem (LP). The BIP problems, which are the most computationally intensive, can be accelerated by quantum computing through solving their equivalent QUBO formulations.

We have evaluated the computational efficiency and solution quality of our method by designing 3D bridges using both single and multiple materials. As it directly handles binary design variables, our method naturally produces clear-cut 0/1 topologies, unlike SIMP [19], the predominant TO approach, which relaxes binary variables into continuous ones (varying between 0 and 1) and requires post-processing, such as Heaviside projection [47], to revert to binary representations. In its classical implementation, our method achieves comparable objective function values while reducing overall computation time by at least an order of magnitude compared to SIMP [19]. When benchmarked against DVTO-MT [20] on the time required for solving the master problems, the present method can achieve speedups from one to three orders of magnitude. Remarkably, the MDW decomposition maintains low computational time even for the largest problem tested ( $150 \times 600 \times 150$ , yielding 54 million design variables), where the MILP solver fails to return a solution. The proposed quantum implementation has the potential to further accelerate solving the resultant BIP sub-problems by about another order of magnitude. Due to current constraints in accessing real quantum

hardware, we verified the validity of the formulated QUBO using QAOA [45]. All the speedups noted above consistently become more pronounced with increasing problem size and complexity (moving from single-material to multi-material designs). This suggests that the new method and quantum computing will play an increasingly valuable role in addressing the scale and complexity of real-world TO applications.

Another important advantage of the proposed MDW decomposition is that each resulting BIP (local sub-problem) involves only local constraints. As a result, the corresponding QUBO formulation features a sparse Hamiltonian, eliminating the need for all-to-all qubit connectivity, a key consideration for near-term quantum hardware. Additionally, each local sub-problem can be solved independently within each MDW iteration, allowing all QUBOs to be processed in parallel.

It is also important to note that our estimates of quantum speedup include the time required to construct the QUBO problem,  $T_{\text{QUBO}}$ , i.e., the time to generate the QUBO's coefficient matrix  $\mathbf{Q}$ . Since our method allows  $\mathbf{Q}$  to be sparse,  $T_{\text{QUBO}}$  should theoretically scale linearly with the problem size. However, practical code implementation can affect the actual scalability of  $T_{\text{QUBO}}$ . To achieve the desired linear scalability for  $T_{\text{QUBO}}$ , an improved code implementation is necessary, as discussed in §4.3. With this improvement, we anticipate an even more substantial quantum speedup.

In this work, we have focused on reducing both the total number of iterations and the time required to solve the optimization sub-problems at each iteration. By decreasing the iteration count, we have effectively reduced the number of repeated PDE solves, thereby lowering the overall time spent on PDE solving. Further improvements in efficiency are expected if the per-iteration PDE solving can also be accelerated. To this end, integrating quantum-accelerated PDE solvers [48–50] into TO represents a promising direction for future work, offering the potential to further enhance the efficiency and scalability of TO.

## Acknowledgment

This work was supported by the University of Wisconsin - Madison Office of the Vice Chancellor for Research and Graduate Education with funding from the Wisconsin Alumni Research Foundation.

## References

- [1] J. Wu, O. Sigmund, and J. P. Groen, “Topology optimization of multi-scale structures: a review,” *Structural and Multidisciplinary Optimization*, vol. 63, pp. 1455–1480, 2021.
- [2] T. Borrvall and J. Petersson, “Topology optimization of fluids in Stokes flow,” *International journal for numerical methods in fluids*, vol. 41, no. 1, pp. 77–107, 2003.
- [3] A. Gersborg-Hansen, O. Sigmund, and R. B. Haber, “Topology optimization of channel flow problems,” *Structural and multidisciplinary optimization*, vol. 30, no. 3, pp. 181–192, 2005.
- [4] S. Kreissl, G. Pingen, and K. Maute, “Topology optimization for unsteady flow,” *International Journal for Numerical Methods in Engineering*, vol. 87, no. 13, pp. 1229–1253, 2011.
- [5] G. Kiziltas, D. Psychoudakis, J. L. Volakis, and N. Kikuchi, “Topology design optimization of dielectric substrates for bandwidth improvement of a patch antenna,” *IEEE Transactions on Antennas and Propagation*, vol. 51, no. 10, pp. 2732–2743, 2003.
- [6] T. Nomura, K. Sato, K. Taguchi, T. Kashiwa, and S. Nishiwaki, “Structural topology optimization for the design of broadband dielectric resonator antennas using the finite difference time domain technique,” *International Journal for Numerical Methods in Engineering*, vol. 71, no. 11, pp. 1261–1296, 2007.

- [7] E. M. Dede, “Multiphysics topology optimization of heat transfer and fluid flow systems,” in *proceedings of the COMSOL Users Conference*, vol. 715, 2009.
- [8] S. Kreissl, G. Pingen, A. Evgrafov, and K. Maute, “Topology optimization of flexible micro-fluidic devices,” *Structural and Multidisciplinary Optimization*, vol. 42, no. 4, pp. 495–516, 2010.
- [9] P. Kumar, J. S. Frouws, and M. Langelaar, “Topology optimization of fluidic pressure-loaded structures and compliant mechanisms using the Darcy method,” *Structural and Multidisciplinary Optimization*, vol. 61, no. 4, pp. 1637–1655, 2020.
- [10] M. Cavazzuti, A. Baldini, E. Bertocchi, D. Costi, E. Torricelli, and P. Moruzzi, “High performance automotive chassis design: a topology optimization based approach,” *Structural and Multidisciplinary Optimization*, vol. 44, pp. 45–56, 2011.
- [11] J.-H. Zhu, W.-H. Zhang, and L. Xia, “Topology optimization in aircraft and aerospace structures design,” *Archives of computational methods in engineering*, vol. 23, pp. 595–622, 2016.
- [12] P. Belotti, C. Kirches, S. Leyffer, J. Linderoth, J. Luedtke, and A. Mahajan, “Mixed-integer nonlinear optimization,” *Acta Numerica*, vol. 22, p. 1–131, 2013.
- [13] E. Andreassen, A. Clausen, M. Schevenels, B. S. Lazarov, and O. Sigmund, “Efficient topology optimization in MATLAB using 88 lines of code,” *Structural and Multidisciplinary Optimization*, vol. 43, no. 1, pp. 1–16, 2011.
- [14] Y. Liang and G. Cheng, “Topology optimization via sequential integer programming and canonical relaxation algorithm,” *Computer Methods in Applied Mechanics and Engineering*, vol. 348, pp. 64–96, 2019.
- [15] R. Picelli, R. Sivapuram, and Y. M. Xie, “A 101-line MATLAB code for topology optimization using binary variables and integer programming,” *Structural and Multidisciplinary Optimization*, vol. 63, no. 2, pp. 935–954, 2021.
- [16] E. Muñoz and M. Stolpe, “Generalized Benders’ decomposition for topology optimization problems,” *Journal of Global Optimization*, vol. 51, no. 1, pp. 149–183, 2011.
- [17] X. Huang and W. Li, “A new multi-material topology optimization algorithm and selection of candidate materials,” *Computer Methods in Applied Mechanics and Engineering*, vol. 386, p. 114114, 2021.
- [18] H. Liu, C. Wang, Y. Zhang, and Y. Liang, “Multi-material structural discrete variable topology optimization with minimum length scale control under mass constraint,” *Computer Methods in Applied Mechanics and Engineering*, vol. 420, p. 116701, 2024.
- [19] Y. Jia, C. Wang, and X. S. Zhang, “FEniTop: a simple FEniCSx implementation for 2D and 3D topology optimization supporting parallel computing,” *Structural and Multidisciplinary Optimization*, vol. 67, no. 8, p. 140, 2024.
- [20] Z. Ye and W. Pan, “Discrete variable topology optimization using multi-cut formulation and adaptive trust regions,” *Structural and Multidisciplinary Optimization*, vol. 68, no. 2, p. 25, 2025.
- [21] Z. Ye, X. Qian, and W. Pan, “Quantum topology optimization via quantum annealing,” *IEEE Transactions on Quantum Engineering*, vol. 4, 2023.
- [22] T. Albash and D. A. Lidar, “Adiabatic quantum computation,” *Reviews of Modern Physics*, vol. 90, no. 1, p. 015002, 2018.

- [23] A. Ajagekar, K. Al Hamoud, and F. You, “Hybrid classical-quantum optimization techniques for solving mixed-integer programming problems in production scheduling,” *IEEE Transactions on Quantum Engineering*, vol. 3, pp. 1–16, 2022.
- [24] A. Guillaume, E. Y. Goh, M. D. Johnston, B. D. Wilson, A. Ramanan, F. Tibble, and B. Lackey, “Deep space network scheduling using quantum annealing,” *IEEE Transactions on Quantum Engineering*, vol. 3, pp. 1–13, 2022.
- [25] K. A. H. Kelany, N. Dimopoulos, C. P. Adolphs, and A. Baniyasi, “Quantum annealing methods and experimental evaluation to the phase-unwrapping problem in synthetic aperture radar imaging,” *IEEE Transactions on Quantum Engineering*, vol. 3, pp. 1–20, 2022.
- [26] S. Heng, D. Kim, T. Kim, and Y. Han, “How to solve combinatorial optimization problems using real quantum machines: A recent survey,” *IEEE Access*, vol. 10, pp. 120 106–120 121, 2022.
- [27] X. Liu, A. Angone, R. Shaydulin, I. Safro, Y. Alexeev, and L. Cincio, “Layer VQE: A variational approach for combinatorial optimization on noisy quantum computers,” *IEEE Transactions on Quantum Engineering*, vol. 3, pp. 1–20, 2022.
- [28] P. Ray, B. K. Chakrabarti, and A. Chakrabarti, “Sherrington-kirkpatrick model in a transverse field: Absence of replica symmetry breaking due to quantum fluctuations,” *Physical Review B*, vol. 39, no. 16, p. 11828, 1989.
- [29] T. Kadowaki and H. Nishimori, “Quantum annealing in the transverse ising model,” *Physical Review E*, vol. 58, no. 5, p. 5355, 1998.
- [30] J. Preskill, “Quantum Computing in the NISQ era and beyond,” *Quantum*, vol. 2, p. 79, 2018.
- [31] Y. Kim, C. J. Wood, T. J. Yoder, S. T. Merkel, J. M. Gambetta, K. Temme, and A. Kandala, “Scalable error mitigation for noisy quantum circuits produces competitive expectation values,” *Nature Physics*, vol. 19, pp. 752–759, 2023.
- [32] “D-Wave system documentation,” 2022. [Online]. Available: <https://docs.dwavesys.com/docs/latest/index.html>
- [33] G. B. Dantzig and P. Wolfe, “Decomposition principle for linear programs,” *Operations research*, vol. 8, no. 1, pp. 101–111, 1960.
- [34] X. Wang, Z. Wang, and B. Ni, “Mapping structural topology optimization problems to quantum annealing,” *Structural and Multidisciplinary Optimization*, vol. 67, no. 5, p. 74, 2024.
- [35] R. Honda, K. Endo, T. Kaji, Y. Suzuki, Y. Matsuda, S. Tanaka, and M. Muramatsu, “Development of optimization method for truss structure by quantum annealing,” *Scientific reports*, vol. 14, no. 1, p. 13872, 2024.
- [36] N. Sukulthanasorn, J. Xiao, K. Wagatsuma, R. Nomura, S. Moriguchi, and K. Terada, “A novel design update framework for topology optimization with quantum annealing: Application to truss and continuum structures,” *Computer Methods in Applied Mechanics and Engineering*, vol. 437, p. 117746, 2025.
- [37] M. P. Bendsoe and O. Sigmund, *Topology optimization: theory, methods, and applications*. Springer Science & Business Media, 2013.
- [38] J. Nocedal and S. J. Wright, *Numerical optimization*. Springer, 1999.
- [39] K. Sun, Y. Liang, and G. Cheng, “Sensitivity analysis of discrete variable topology optimization,” *Structural and Multidisciplinary Optimization*, vol. 65, no. 8, pp. 1–18, 2022.

- [40] A. Reuss, “Berechnung der fließgrenze von mischkristallen auf grund der plastizitätsbedingung für einkristalle .” *ZAMM - Journal of Applied Mathematics and Mechanics / Zeitschrift für Angewandte Mathematik und Mechanik*, vol. 9, no. 1, pp. 49–58, 1929.
- [41] B. S. Lazarov and O. Sigmund, “Filters in topology optimization based on helmholtz-type differential equations,” *International journal for numerical methods in engineering*, vol. 86, no. 6, pp. 765–781, 2011.
- [42] Gurobi Optimization, LLC, “Gurobi optimizer reference manual,” 2022. [Online]. Available: <https://www.gurobi.com>
- [43] I. A. Baratta, J. P. Dean, J. S. Dokken, M. Habera, J. S. Hale, C. N. Richardson, M. E. Rognes, M. W. Scroggs, N. Sime, and G. N. Wells, “DOLFINx: the next generation FEniCS problem solving environment,” preprint, 2023.
- [44] A. B. Yoo, M. A. Jette, and M. Grondona, “Slurm: Simple linux utility for resource management,” in *Workshop on job scheduling strategies for parallel processing*. Springer, 2003, pp. 44–60.
- [45] The CUDA-Q development team, “CUDA-Q.” [Online]. Available: <https://github.com/NVIDIA/cuda-quantum>
- [46] A. Maruo, T. Soeda, and H. Igarashi, “Topology optimization of electromagnetic devices using digital annealer,” *IEEE Transactions on Magnetics*, vol. 58, no. 9, pp. 1–4, 2022.
- [47] A. Kawamoto, T. Matsumori, S. Yamasaki, T. Nomura, T. Kondoh, and S. Nishiwaki, “Heaviside projection based topology optimization by a PDE-filtered scalar function,” *Struct. Multidiscip. Optim.*, vol. 44, pp. 19–24, 2011.
- [48] A. W. Harrow, A. Hassidim, and S. Lloyd, “Quantum algorithm for linear systems of equations,” *Physical Review Letters*, vol. 103, no. 15, p. 150502, 2009.
- [49] Y. Subaşı, R. D. Somma, and D. Orsucci, “Quantum algorithms for systems of linear equations inspired by adiabatic quantum computing,” *Physical review letters*, vol. 122, no. 6, p. 060504, 2019.
- [50] O. M. Raisuddin and S. De, “FEqa: Finite element computations on quantum annealers,” *Computer Methods in Applied Mechanics and Engineering*, vol. 395, p. 115014, 2022.